INTERNATIONAL ATOMIC ENERGY AGENCY
UNITED NATIONS EDUCATIONAL, SCIENTIFIC AND CULTURAL ORGANIZATION

INTERNATIONAL CENTRE FOR THEORETICAL PHYSICS
34100 TRIESTE (ITALY) - P.O.B. 586 - MIRAMARE - STRADA COSTIERA 11 - TELEPHONE: 2240-1
CABLE: CENTRATOM - TELEX 460392 - I

SMR/388 - 15

SPRING COLLEGE IN MATERIALS SCIENCE
ON
"CERAMICS AND COMPOSITE MATERIALS"
(17 April - 26 May 1989)

ELECTRON MICROSCOPY
(Lectures V-VIII, continued)

M.J. GORINGE
Department of Metallurgy and
Science of Materials
Parks Road
Oxford OX1 3PH
UK

Electron Microscopy – Lectures 5–8 (cont)

M.J. Goringe

Double Diffraction

5/8

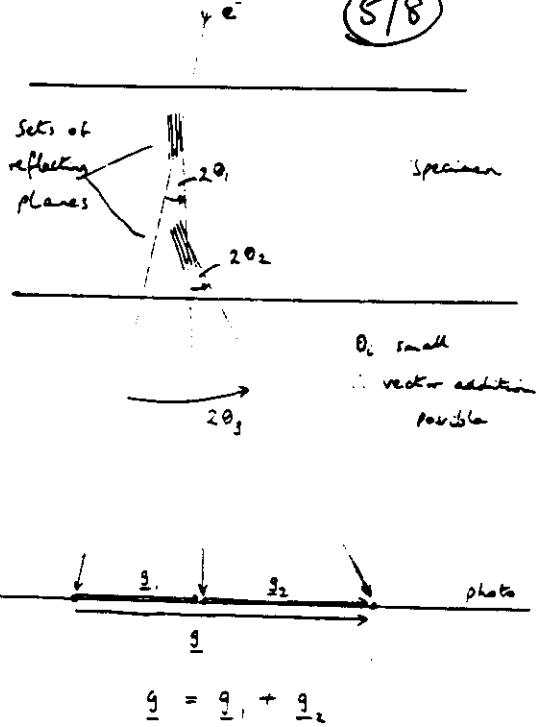

$\underline{g} = \underline{g}_1 + \underline{g}_2$

In general not colinear

e.g. 002 = $\bar{1}11$ + $1\bar{1}1$ all = [110]

Deviation Parameter, S_g

5/13b

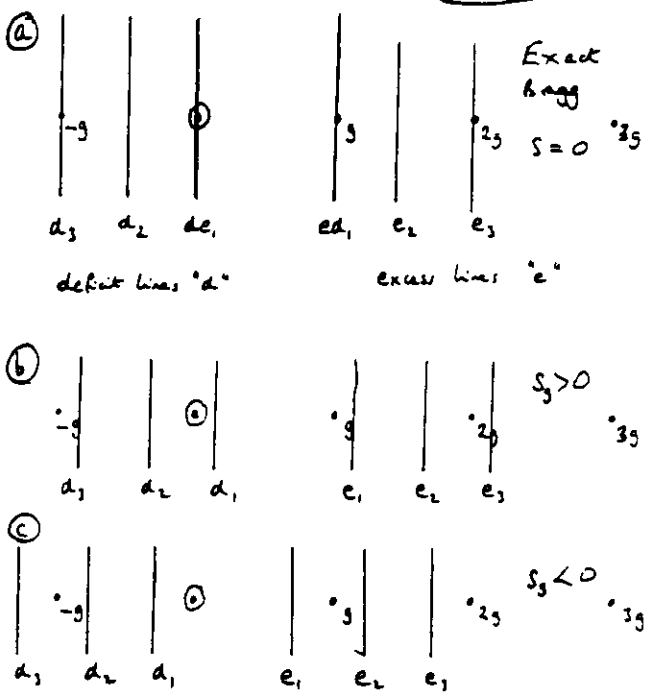

5/15

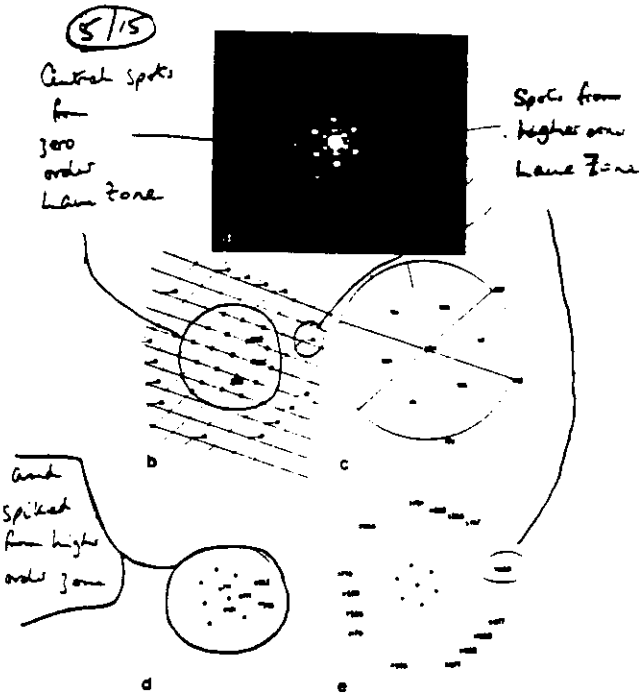

5/16

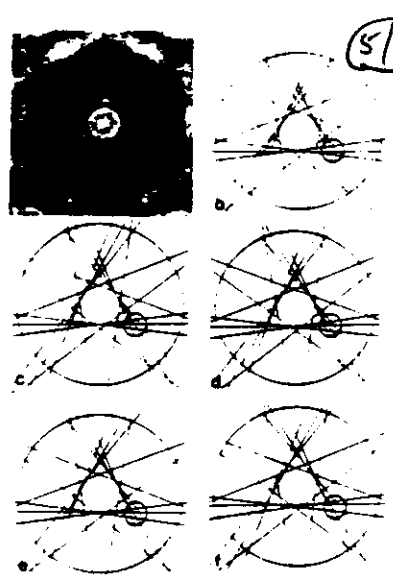

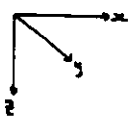

6/1a

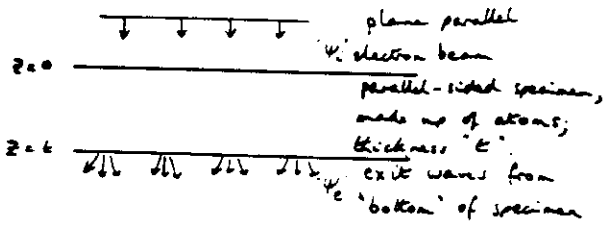

Q. What happens to the wave(s) inside the specimen?

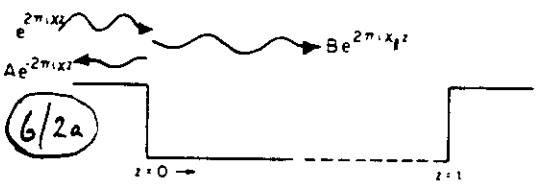

6/2a

Schematic representation of an electron wave entering a specimen, suffering some reflection of amplitude A.

PG – Phase grating approach (cf physical optics)

Kin – Kinematical scattering approach (cf. x-ray diffraction)

Block – Block wave approach (cf electrons in solids)

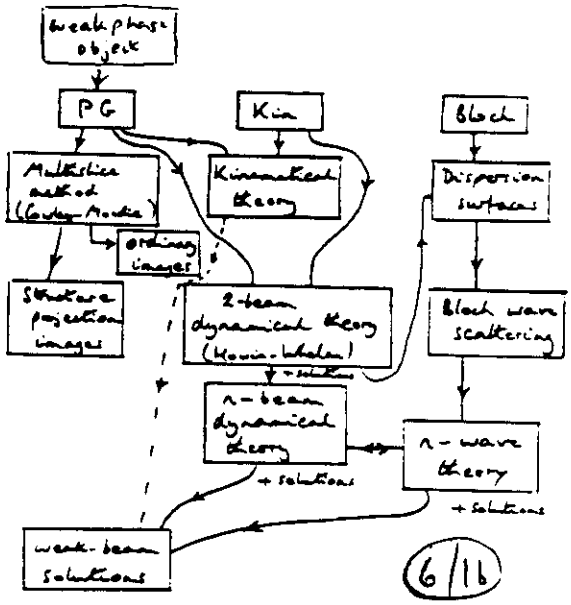

6/1b

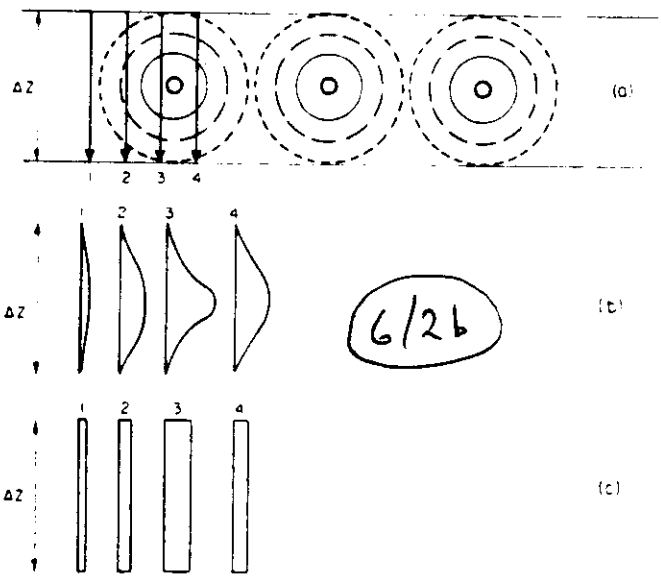

6/2b

6/2c

Lattice Potential as a Fourier Series (1-D)

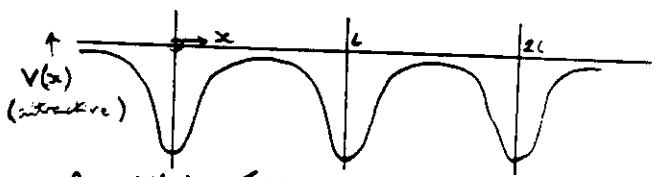

Set $V(x) = \sum_n V_n \exp(2\pi i n x/l)$ or $\begin{cases}\cos\\ \sin\end{cases}$

$$\int_0^l V(x)\exp(-2\pi i m x/l)\,dx = \int_0^l \sum_n V_n \exp[2\pi i(n-m)x/l]\,dx$$

$$RHS = \sum_n V_n \int_0^l \exp[2\pi i(n-m)x/l]\,dx$$

$$= \sum_n V_n \left[\frac{\exp[2\pi i(n-m)x/l]}{2\pi i(n-m)/l}\right]_0^l$$

$$= V_m \quad (\text{the bracket} = 0 \text{ for } m \neq n)$$

ie $$V_m = \int_0^l V(x)\exp(-2\pi i m x/l)\,dx$$

If $V(x)$ is centrosymmetric

$$V_m = \int_0^l V(x)\cos(2\pi m x/l)\,dx$$

For most reasonable potentials V_n is a decreasing function of the order n.

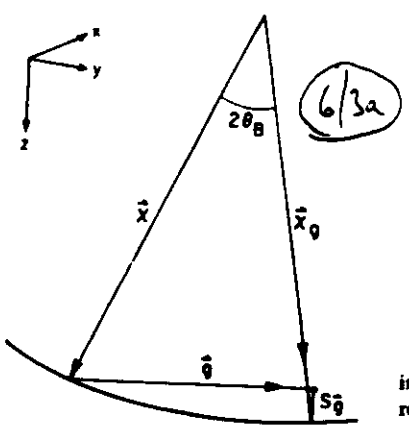

6/3a

The Ewald sphere construction, relating incident wave of wave vector x, diffracted wave x, reflecting vector g, and deviation parameter s_g.

6/3b

Extinction Distances and Absorption Lengths (nm) for 100 keV Electrons Used in Calculations for Typical Light, Medium, and Heavy Elements[a]

	Light (Aluminum)		Medium (Copper)		Heavy (Gold)	
g	ξ_g	ξ'_g	ξ_g	ξ'_g	ξ_g	ξ'_g
000	(20.0)	886	(15.0)	293	(11.4)	89.8
111	57.3	1000	30.2	410	18.3	107
200	68.3	1100	33.6	430	20.1	112
220	107	1570	45.1	500	26.5	121
222	140	1820	55.6	530	32.5	130
400	168	1930	65.9	599	38.2	132
333	230	2500	92.7	742	53.1	148
444	362	3930	149	851	78.6	175
555	526	5720	223	1210	110	229
666	705	7660	303	1640	145	290

[a] Values based on calculations of Doyle and Turner,[18] Humphreys and Hirsch,[19] and Radi.[20]

6/3c

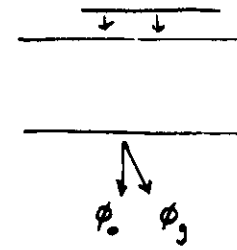

Objective aperture placed to select either ϕ_0 or ϕ_g only. Image on screen is then $I_0 = \phi_0 \phi_0^*$ bright field

or $I_g = \phi_g \phi_g^*$ dark field

Kinematical approximation deals with ϕ_g only ⇒ dark field image image

2-beam dynamical yields both images

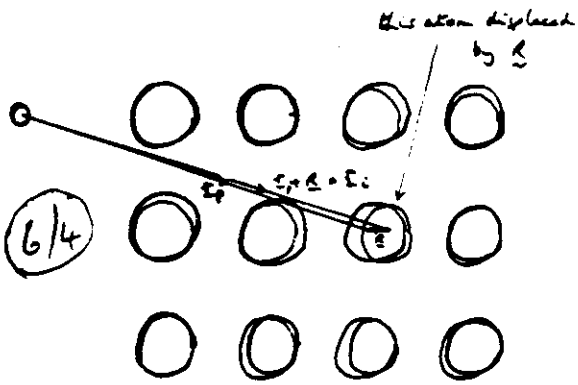

6/4

— perfect crystal

— distorted crystal

$$V(r_i) = V(\underline{r}_i - \underline{R}) = V(\underline{r}_p)$$

$$\Delta s = g \Delta\theta = \underline{g} \cdot \frac{d\underline{R}}{dt} = \beta'$$

6/5b

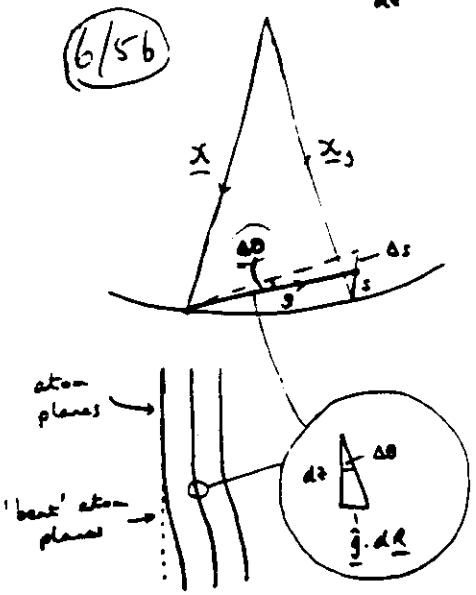

Kinematical scattering

6/5a

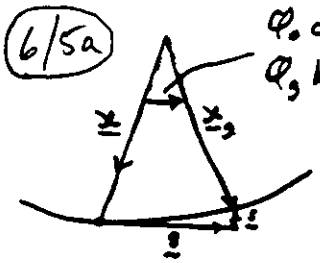

ϕ_0 changes, is absorbed + scatters into ϕ_g.

ϕ_g builds up — ϕ_g (4.19) but is also absorbed.

Reverse "kinematical" scattering

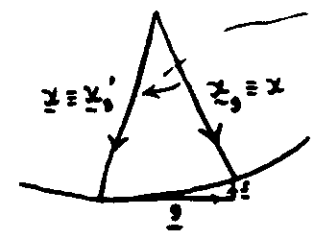

ϕ_g acts like ϕ_0 above

ϕ_0 acts like ϕ_g above except signs of both $\underline{g}$ — $\underline{s}$ reversed

Dynamical scattering and includes "absorption"

Combine the two, to yield eqns (4.20)

6/6a

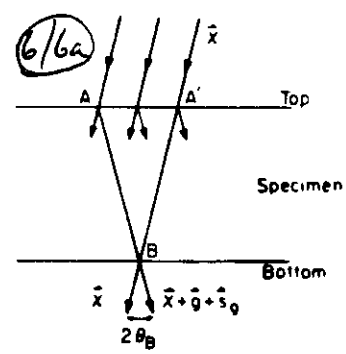

An electron microscope specimen, illustrating how only information in the triangle $AA'B$ may be present in the electron beams emitted at the lower surface at B.

6/6b

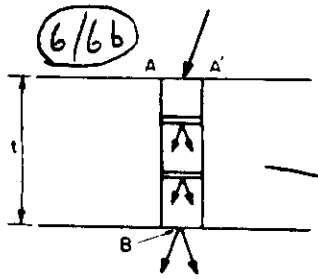

Illustrating the column approximation.

6/6c

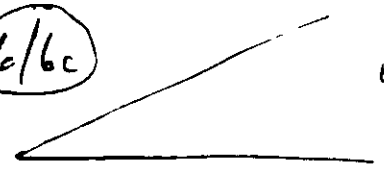

tapered crystal

equivalent to

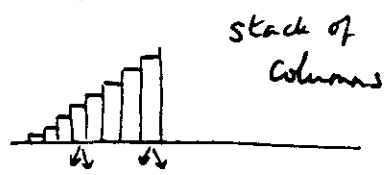

stack of columns

or, neglecting phase differences in the incident wave

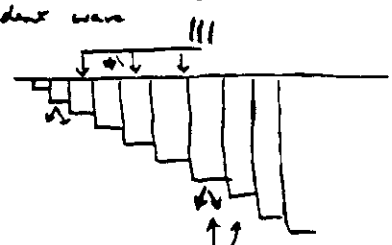

adjacent columns independent of each other

Perfect Crystal Solutions

6/7a

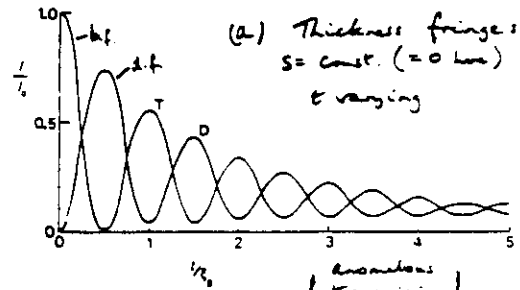

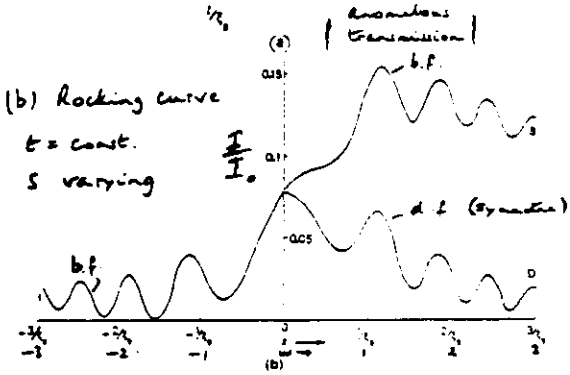

(a) Calculated thickness fringe profiles for transmitted (T) and diffracted (D) waves, including absorption: $\xi_g = 10\xi_0$, $\xi_0' = 15\xi_g$. (b) transmitted and diffracted intensities as a function of orientation (rocking curves) for a thickness of $\frac{1}{2}\xi_g$ and the same absorption parameters. The bright-field asymmetry is evident.

6/7c (a) bright field (b) dark field $\underline{g}$

⟷ bent ↓ thickness increasing

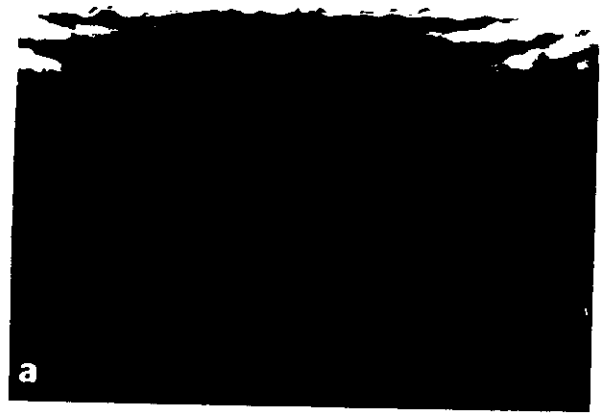

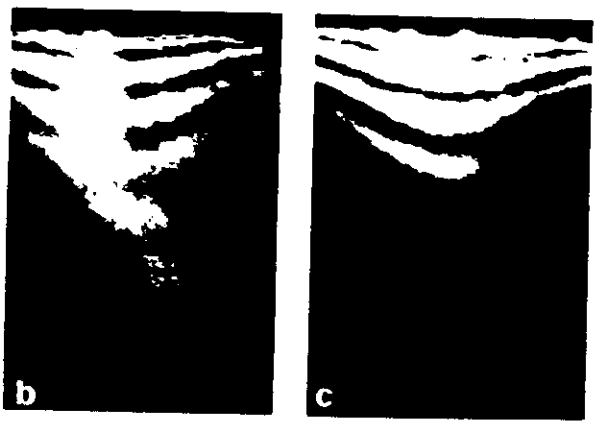

6/7b (a) bright field

(b), (c) $+\underline{g}$, $-\underline{g}$ dark field

↓ thickness increasing

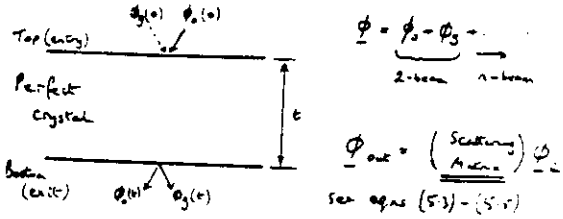

$\phi = \phi_o - \phi_g$ → 2-beam, n-beam

$\phi_{out} = \left(\frac{\text{Scattering}}{\text{Matrix}}\right)\phi_{in}$

See eqns (5·3) – (5·7)

7/1

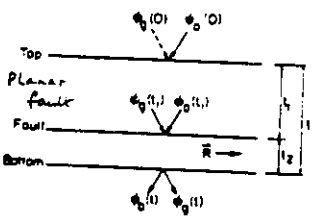

Lower part of crystal displaced by $\bar{R}$

Phase angle $\alpha = 2\pi \underline{g}.\underline{R}$

See eqns (5·6) – (5·12)

7/2a

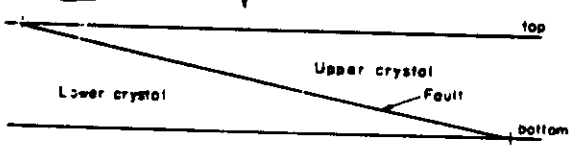

fault cuts entrance surface at "top"

fault cuts exit surface at "bottom"

7/2b

$\alpha = +\frac{2\pi}{3}$

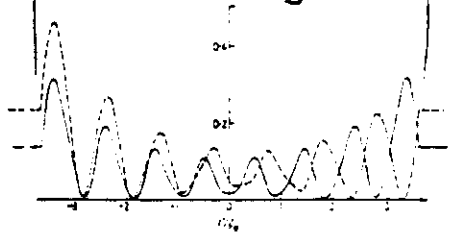

Figure 10.3. Computed stacking fault image profile for $\alpha = -2\pi/3$ with and without absorption effects included. $\xi_g = 1{\cdot}25$, $\xi_g' = \xi_0' = \xi_0 \xi_g' = 0{\cdot}075$, $w = 0{\cdot}2$. Bright- and dark-field images are shown as continuous and broken lines respectively.

7/2c

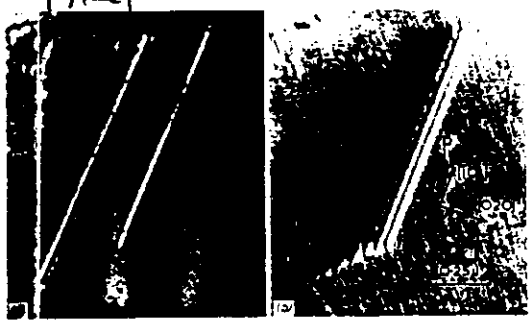

Figure 10.10. Bright-field (a) and dark-field (b) images of a stacking fault with $\alpha = -2\pi/3$ in Cu + 7% Al alloy, [101] orientation. The reflection $\underline{g} = [\bar{1}\bar{1}1]$ is shown. Compare with Figure 10.8.

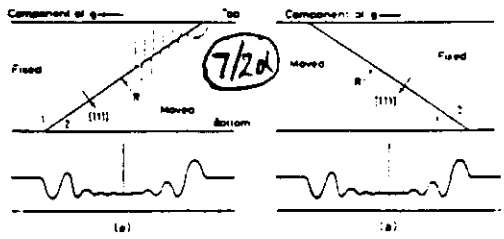

7/2d

Figure 10.12. Possible geometry of the fault shown in Figure 10.10. Comparison of the bright-field and dark-field images enables the edges at top and bottom of the fault to be identified. Relative to the direction of g marked on Figure 10.10, the fault must then run as shown in Figure 10.12a and not as in Figure 10.12b.

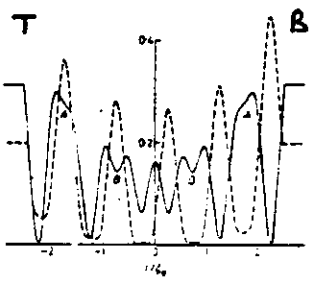

7/2e

$\alpha = -2\pi/3$

Figure 10.9. Computed stacking fault image profile for $\alpha = -2\pi/3$ with anomalous absorption effects included, ($\xi_g = 5$, $\xi_0' = \xi_g' = \xi_0 \xi_g' = 0{\cdot}07$, $w = 0$. Bright- and dark-field images are shown as continuous and broken lines respectively.

7/2f

Micrographs of stacking faults in silicon, $\alpha = \pm 2\pi/3$ and 0, imaged in $\underline{g} = 220$ at 1 MV: (*a*) bright field, (*b*) dark field. Notice defects from displacement damage.

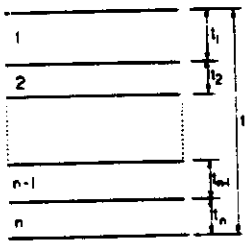

7/3a

Schematic diagram showing a number of faults parallel to the surface.

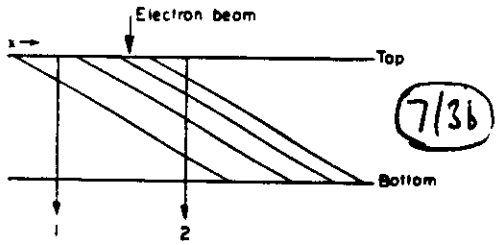

7/3b

Schematic representation of a number of inclined faults.

7/3c

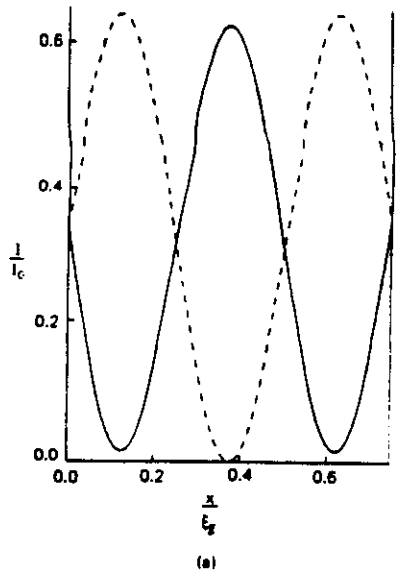

(a)

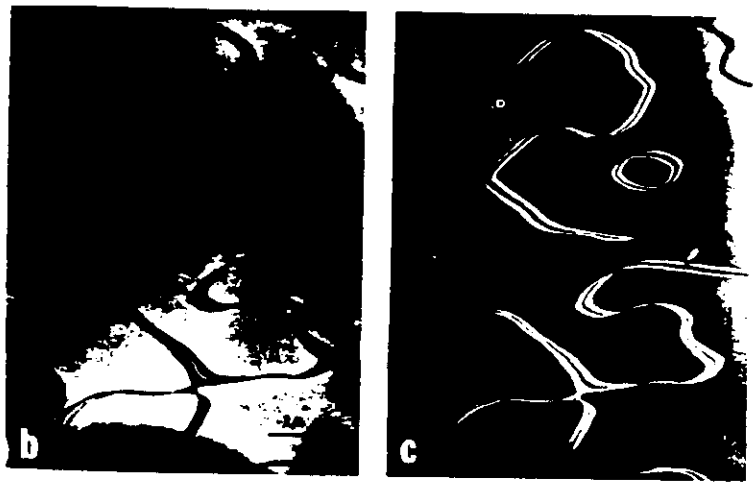

Pi faults in thin crystals. (*a*) Calculated profiles of bright field (solid) and dark field (dashed) intensities ($\xi_g/\xi'_g = \xi_g/\xi'_0 = 0.1$, $t/\xi_g = 0.75$, $\alpha = \pi$). (*b*) Bright field image of antiphase boundaries in anorthite (650 kV electrons). (*c*) Corresponding dark field image. (*b*, *c*)

$$2\pi\mathbf{R} = \mathbf{b}\Phi + \mathbf{b}\frac{\sin 2\Phi}{4(1-\nu)} + (\mathbf{b}\wedge\mathbf{u})\left[\frac{1-2\nu}{2(1-\nu)}\ln r + \frac{\cos 2\Phi}{4(1-\nu)}\right], \qquad (5.19)$$

7/4a

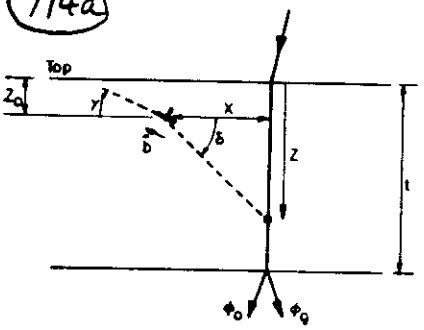

$\Phi = \delta - \gamma$

Example of a suitable coordinate system to describe the strain field of a dislocation.

7/4b Screw dislocation

$\underline{g}\cdot\underline{b} = 1$

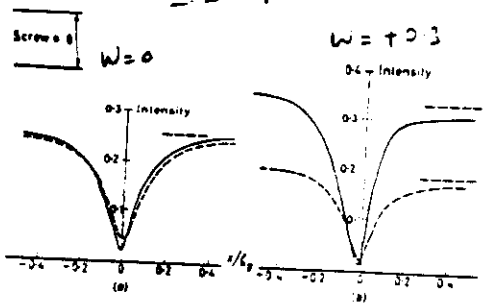

Computed bright-field (continuous line) *and dark-field* (broken line) *images for a screw dislocation in the middle of a thick foil with* $t = 8\xi_g$, $\mathbf{g}\cdot\mathbf{b} = 1$, $\xi_g/\xi'_g = 0.1$. *In* (*a*) $w = 0$; *in* (*b*) $w = 0.3$

image "width" (dark line) $\sim 0.3\,\xi_g$

7/4d

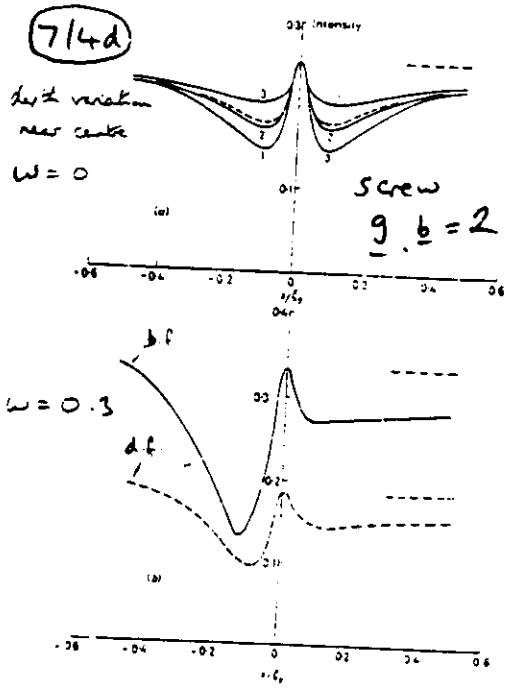

Computed images for a screw dislocation with $\mathbf{g}\cdot\mathbf{b} = 2$, $t = 8\xi_g$, $w = 0$ *in* (*a*), $w = 0.3$ *in* (*b*). *Curves* (*1*), (*2*) *and* (*3*) *in* (*a*) *refer to the dislocation at depths of* $\gamma/\xi_g = 4$, 4.25 *and* 4.5 *respectively*

7/4c $w = 0$

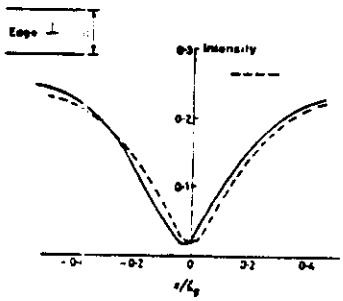

edge disloc

$\underline{g}\cdot\underline{b} = 1$

width $\sim 0.4\,\xi_g$

Computed bright- and dark-field images for an edge dislocation in the middle of a thick foil with $t = 8\xi_g$, $\mathbf{g}\cdot\mathbf{b} = 1$, $\xi_g/\xi'_g = 0.1$, $w = 0$. *Compare with Figure 11.4a*

7/4e

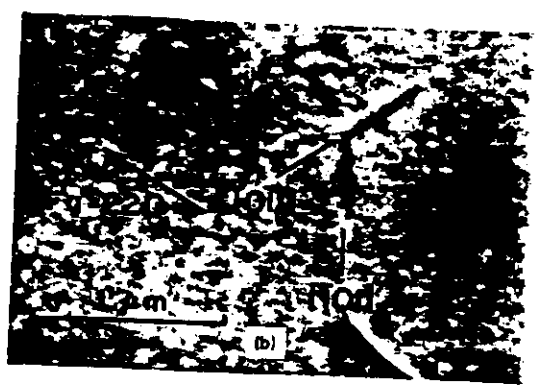

(*b*) Hexagonal Frank loops in copper for which $\mathbf{g}\cdot\mathbf{b} = 0$. Note residual contrast for the directions for which $\mathbf{g}\cdot\mathbf{b}\wedge\mathbf{u}$ is nonzero ($\mathbf{u}$ is the dislocation line direction).

7/4f Depth variation

$\underline{g} \cdot \underline{b} = 1$ Screw

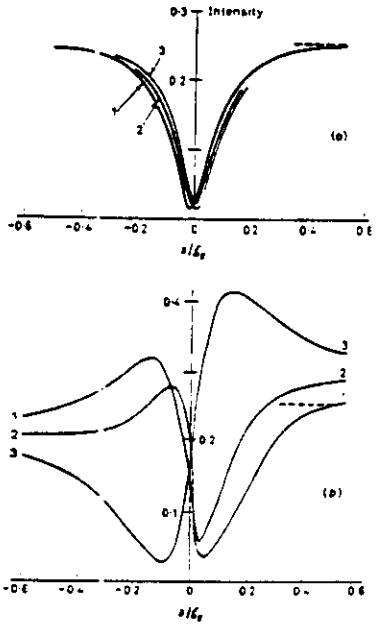

near center

near surface

Figure 11.10. Computed bright-field images for a screw dislocation at varying depths in a foil with $t = 8\xi_g$, $w = 0$, $\xi_g/\xi_g' = 0$; $\underline{g} \cdot \underline{b} = 1$. Curves 1, 2 and 3 refer to $y/\xi_g = 4{\cdot}0$, 4·25 and 4·50 in (a) and to $y/\xi_g = 7{\cdot}25$, 7·50 and 7·75 in (b) when large oscillations occur

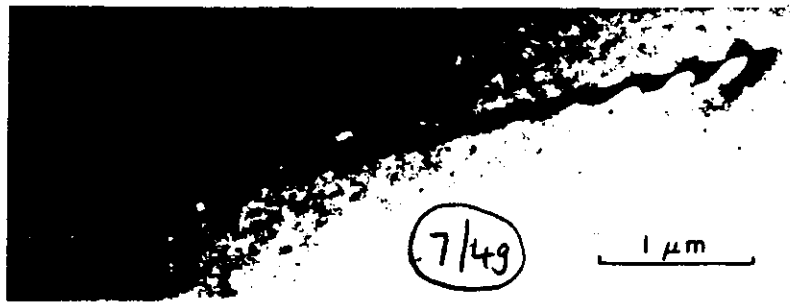

Fig. 5.14 Bright field image of a dislocation threading a specimen from top to bottom. Note the complexity of the image near either surface compared with its simplicity near the center.

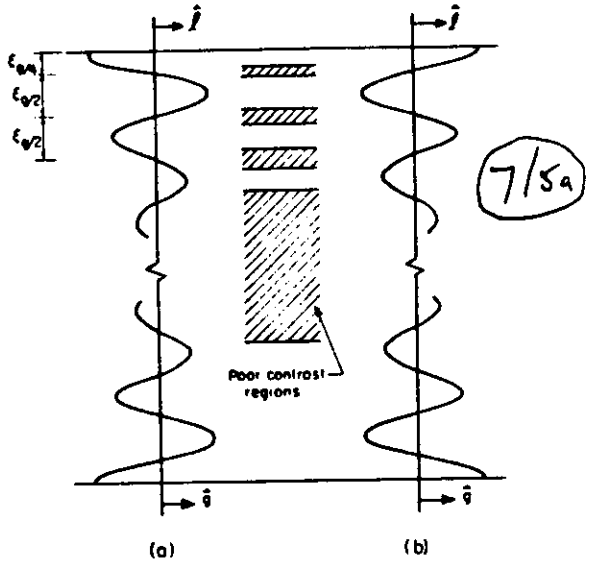

Schematic depth variation in contrast of small defects for orientation near the reflecting position in bright field. The vector l is directed from the black to white contrast lobe.

7/5b

Edge—on loops

C

A

BD

Inclined loops

g: 200

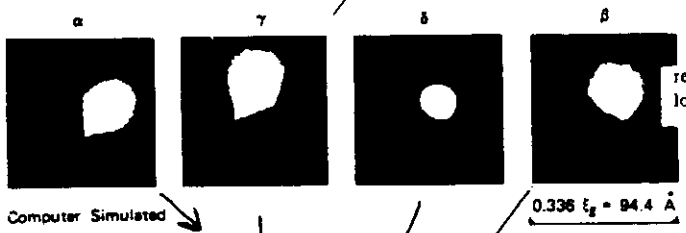

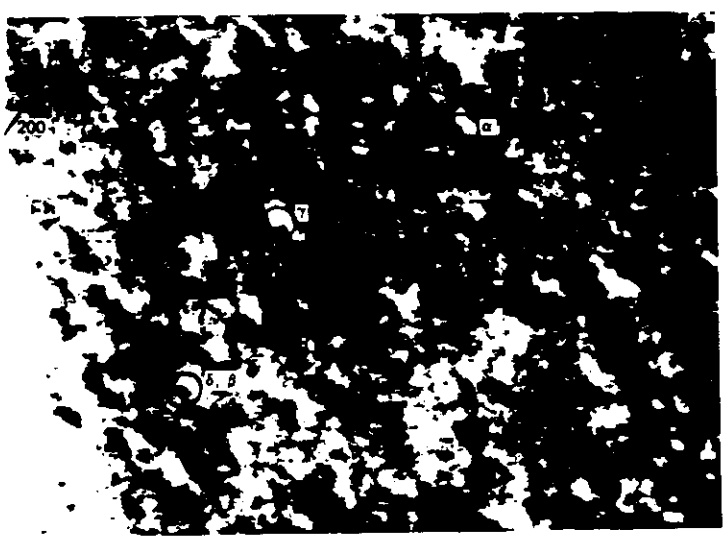

Fig. 5.18 Comparison of images of small Frank loops in ion-bombarded copper. In this particular reflection two out of the four possible configurations may be unambigously identified, other reflections being necessary for the complete analysis.

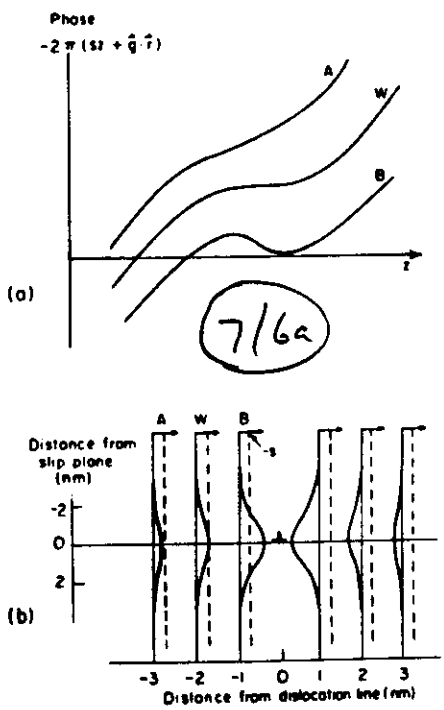

(a) Schematic variation of the phase in the kinematical integral (eq. 5.32) for columns at various positions *A*, *W*, *B* relative to an edge dislocation; see (*b*). (*b*) Variation of β' for columns near an edge dislocation with a typical value of *s* denoted by the dashed line. The rate of change in the phase—see (*a*) – is proportional to $(s + \beta')$ and so is zero when $\beta' = -s$. Courtesy D. J. H. Cockayne.

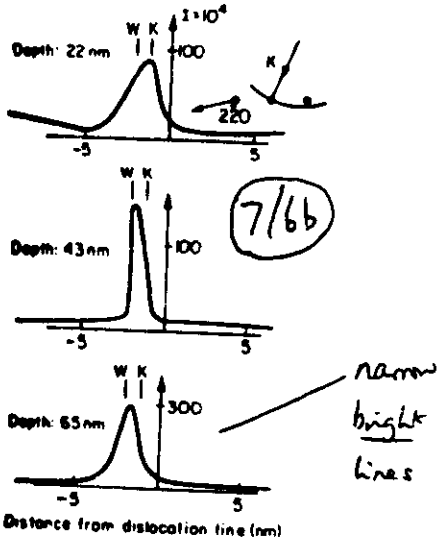

7/6b

narrow bright lines

Many-beam calculated intensity in the weak dark field beam $\mathbf{g} = 2\bar{2}0$ for the orientation indicated in the inset for a dislocation at different depths in a specimen, with the weak beam, *W*, and kinematical, *K*, image positions indicated. Courtesy D. J. H. Cockayne.

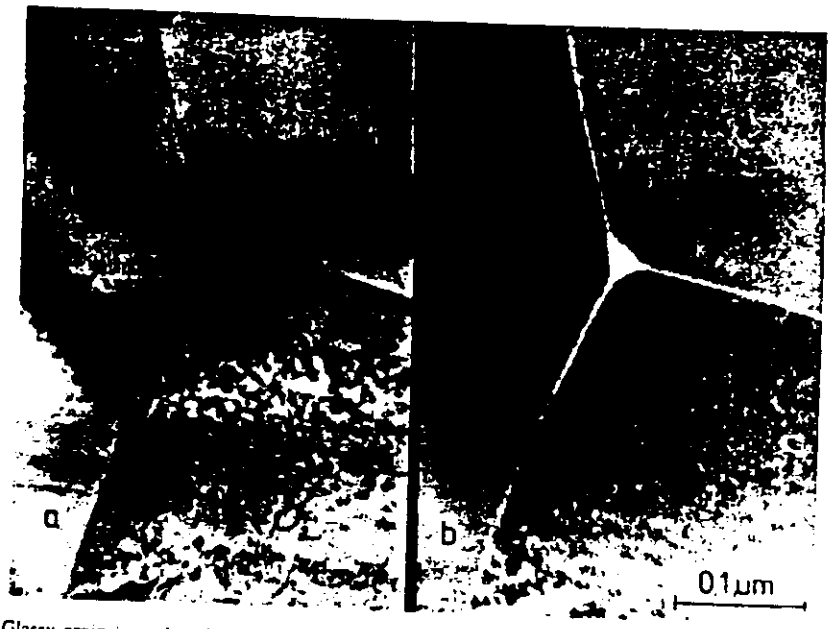

Glassy grain-boundary layer between Al_2O_3 and ZrO_2 (lower right) grains: (*a*) bright field; (*b*) diffuse dark-field contrast.

7/6a

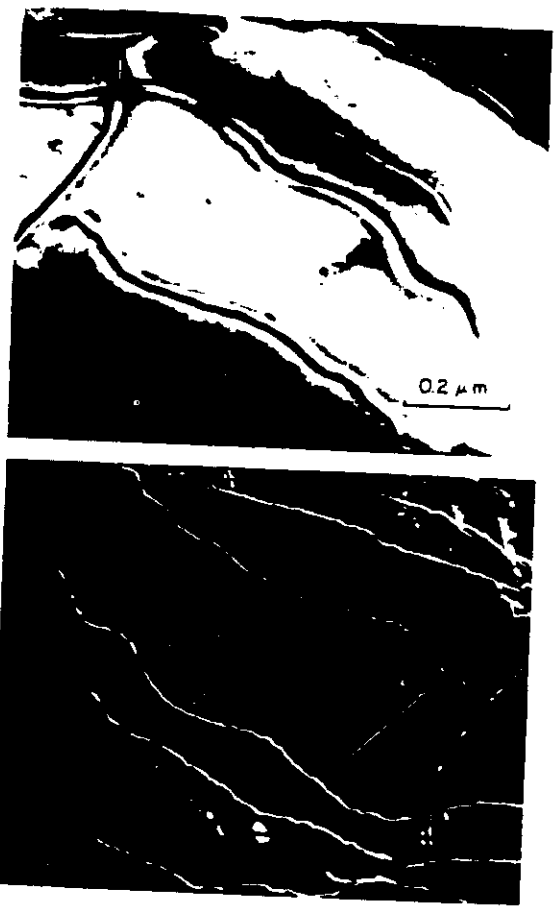

7/6c

7/6d

Showed objective aperture around diffuse scattering from glassy or amorphous phases.

wide, dark line images in either bright or dark field with $s \simeq 0$.

narrow, bright line images in weak beam dark field

Images of disociated dislocations in Cu-10% Al, $\mathbf{b} = \frac{1}{2}[110] - \frac{1}{6}[21\bar{1}] + \frac{1}{6}[121]$ imaged in $\mathbf{g} = 220$, that is, $\mathbf{g} \cdot \mathbf{b} = 2$ with $\mathbf{g} \cdot \mathbf{b}^P = 1$ for each partial dislocation. (*a*) Bright field near the reflecting position. (*b*) Weak beam dark field, showing image width of less than 2 nm. Courtesy C. B. Carter.

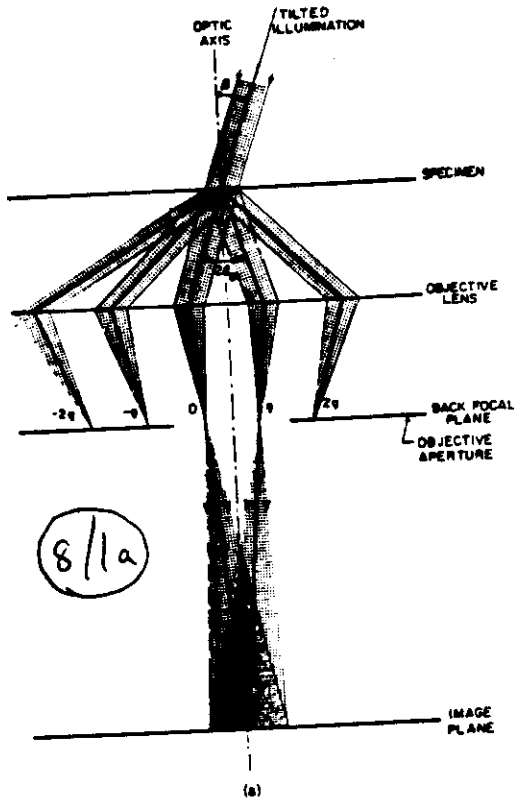

8/1a

(a) Phase contrast imaging from a periodic object. The diffraction pattern is formed in the back focal plane. The period $d = 1/g$ is imaged as magnified fringes if the diffracted and transmitted beams recombine at the image plane (when $2\theta < \alpha$).

8/1b

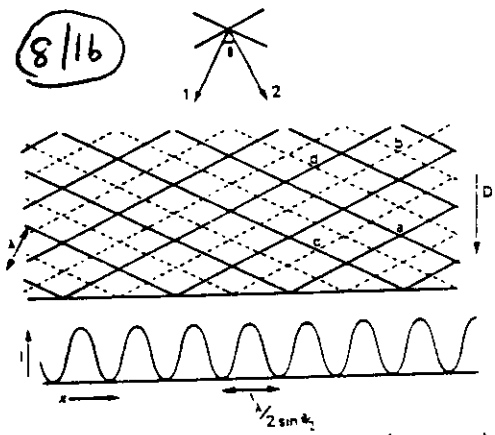

Figure 5.1B. Sketch showing that two coherent sets of waves, numbered 1 and 2, crossing at an angle θ can give rise to fringes on a screen, the spacing of these fringes being $\lambda/2 \sin \theta/2$.

8/1c Moiré fringes from overlapping crystals.

8/2a

Lattice image of a junction between crystalline yttrium-silicon oxynitride grain (*B*) and two Si_3N_4 grains (*A*). There is a narrow amorphous region at *C*, and microledges are resolved at the arrows; these may be sites for crystallization initiation.

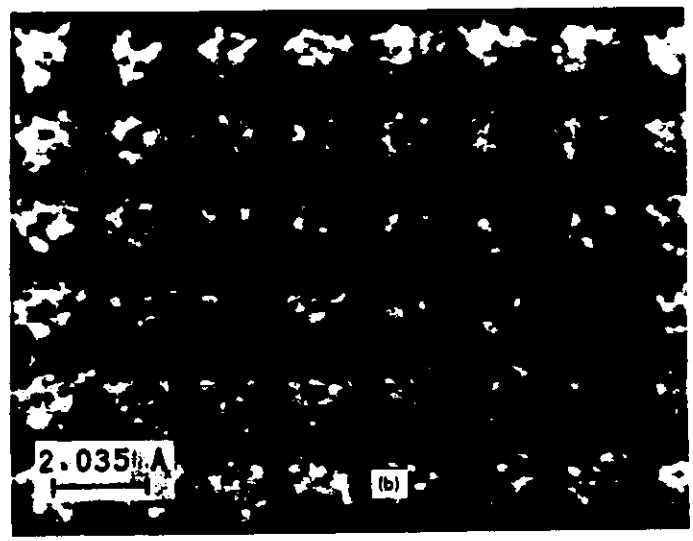

8/2b [100] projection image of gold.

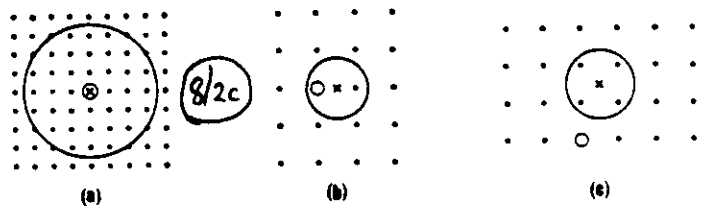

8/2c

Schematic of diffraction pattern/objective aperture configurations for (*a*) structural image, (*b*) two-beam tilted-illumination image, and (*c*) dark field lattice image. The open circle denotes the transmitted beam; the optic axis is located at x.

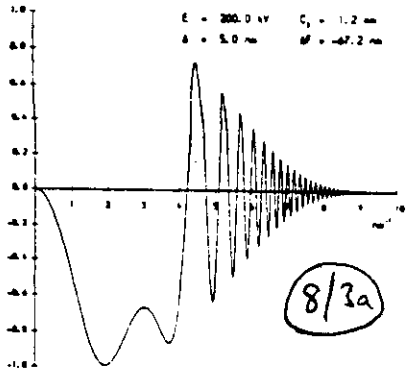

8/3a

CTF for a JEOL 200CX TEM at 1.22Δf

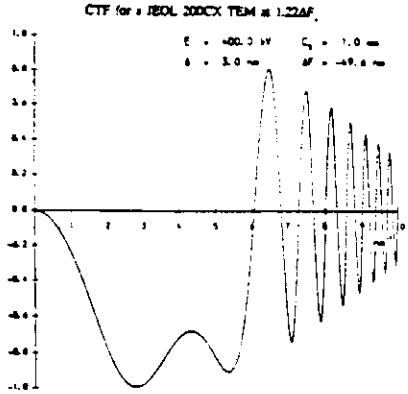

CTF for a JEOL 4000EX TEM at 1.22Δf

8/3b

(a)

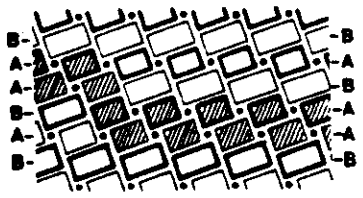

(b)

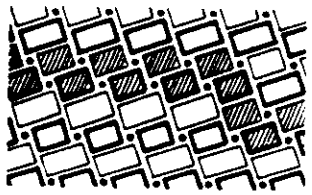

(c)

(*a*) Structure image of H-Nb_2O_5 showing displacement defects. The usual black dots in the overlapping region of two defects (in the rectangular box) can be explained by a superposition of the two different arrangements of structural blocks shown in (*b*) and (*c*).

Other examples shown in lecture 8 from

Pippel E. & Woltersdorf J. "High-voltage and high-resolution electron microscopy studies of interfaces in zirconia-toughened alumina" Phil. Mag. A56, 595–613 (1987).